

## AFM stiffness nanotomography of normal, metaplastic and dysplastic human esophageal cells

This article has been downloaded from IOPscience. Please scroll down to see the full text article.

2011 Phys. Biol. 8 015007

(<http://iopscience.iop.org/1478-3975/8/1/015007>)

View [the table of contents for this issue](#), or go to the [journal homepage](#) for more

Download details:

IP Address: 84.151.236.96

The article was downloaded on 08/02/2011 at 05:17

Please note that [terms and conditions apply](#).

# AFM stiffness nanotomography of normal, metaplastic and dysplastic human esophageal cells

A Fuhrmann<sup>1,4</sup>, J R Staunton<sup>1,4</sup>, V Nandakumar<sup>2</sup>, N Banyai<sup>1</sup>,  
P C W Davies<sup>1,3</sup> and R Ros<sup>1,5</sup>

<sup>1</sup> Department of Physics, Arizona State University, Tempe, AZ 85287, USA

<sup>2</sup> Center for Biosignatures Discovery Automation, Biodesign Institute, Arizona State University, Tempe, AZ 85287, USA

<sup>3</sup> Beyond Center, Arizona State University, Tempe, AZ 85287, USA

E-mail: [robert.ros@asu.edu](mailto:robert.ros@asu.edu)

Received 31 July 2010

Accepted for publication 21 October 2010

Published 7 February 2011

Online at [stacks.iop.org/PhysBio/8/015007](http://stacks.iop.org/PhysBio/8/015007)

## Abstract

The mechanical stiffness of individual cells is important in tissue homeostasis, cell growth, division and motility, and the epithelial–mesenchymal transition in the initiation of cancer. In this work, a normal squamous cell line (EPC2) and metaplastic (CP-A) as well as dysplastic (CP-D) Barrett's Esophagus columnar cell lines are studied as a model of pre-neoplastic progression in the human esophagus. We used the combination of an atomic force microscope (AFM) with a scanning confocal fluorescence lifetime imaging microscope to study the mechanical properties of single adherent cells. Sixty four force indentation curves were taken over the nucleus of each cell in an  $8 \times 8$  grid pattern. Analyzing the force indentation curves, indentation depth-dependent Young's moduli were found for all cell lines. Stiffness tomograms demonstrate distinct differences between the mechanical properties of the studied cell lines. Comparing the stiffness for indentation forces of 1 nN, most probable Young's moduli were calculated to 4.7 kPa for EPC2 ( $n = 18$  cells), 3.1 kPa for CP-A ( $n = 10$ ) and 2.6 kPa for CP-D ( $n = 19$ ). We also tested the influence of nuclei and nucleoli staining organic dyes on the mechanical properties of the cells. For stained EPC2 cells ( $n = 5$ ), significant stiffening was found (9.9 kPa), while CP-A cells ( $n = 5$ ) showed no clear trend (2.9 kPa) and a slight softening was observed (2.1 kPa) in the case of CP-D cells ( $n = 16$ ). Some force–indentation curves show non-monotonic discontinuities with segments of negative slope, resembling a sawtooth pattern. We found the incidence of these 'breakthrough events' to be highest in the dysplastic CP-D cells, intermediate in the metaplastic CP-A cells and lowest in the normal EPC2 cells. This observation suggests that the microscopic explanation for the increased compliance of cancerous and pre-cancerous cells may lie in their susceptibility to 'crumble and yield' rather than their ability to 'bend and flex'.

 Online supplementary data available from [stacks.iop.org/PhysBio/8/015007/mmedia](http://stacks.iop.org/PhysBio/8/015007/mmedia)

## 1. Introduction

The mechanical stiffness of individual cells is important in tissue homeostasis [1], cell growth, division and motility [2, 3], and the epithelial–mesenchymal transition in the

<sup>4</sup> A Fuhrmann and J R Staunton contributed equally to this work.

<sup>5</sup> Author to whom any correspondence should be addressed.

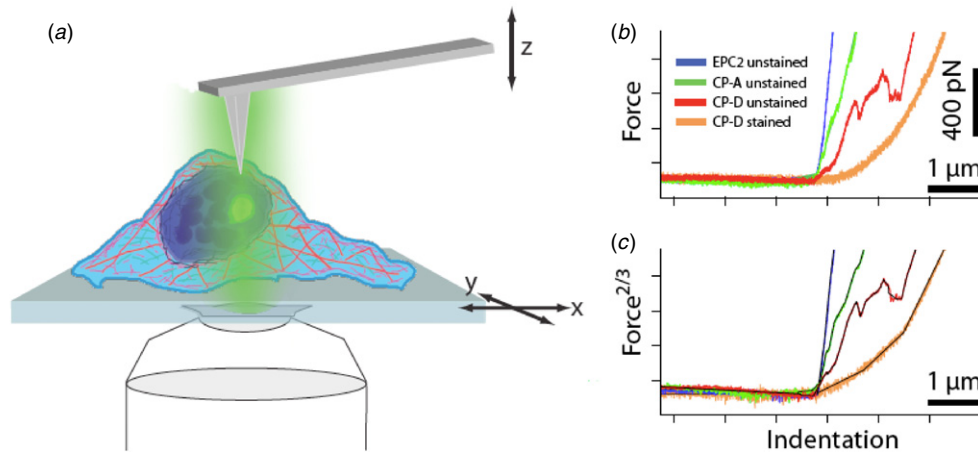


**Figure 1.** Schematic of cell indentation with combined AFM–CLSM setup and force–indentation curves. (a) A sample scanning AFM with piconewton force resolution and nanometer spatial resolution is mounted on a dual color confocal fluorescence microscope with the capability to measure fluorescence lifetimes of the fluorophores (fluorescence lifetime imaging microscopy, FLIM). The AFM tip is aligned with the confocal volume, enabling simultaneous optical and force measurement in a single scan. Each indentation generates a force–indentation ( $F$ – $\delta$ ) curve, four of which are plotted in (b). According to the Hertz model, the Young’s modulus  $E$  is directly proportional to the force  $F$  and inversely proportional to the  $3/2$  power of the deformation  $\delta$ . Consequently, in (c) we plot  $F^{2/3}$  against  $\delta$  and implement a piecewise linear fitting algorithm on the  $F^{2/3}$ – $\delta$  curves. Hertzian behavior corresponds to a single straight line, such as in the EPC2 curve. Changes in slope, such as in the CP-A and CP-D stained curves, reflect changes in  $E(\delta)$  with increasing indentation depth, corresponding to non-Hertzian behavior. Negative slopes, such as in the CP-D unstained curve, reflect cytoskeletal instabilities (see figure 6).

initiation of cancer [4]. Various techniques have been applied to study the mechanical properties of cancer cells (for a comprehensive review, see [5]). Guck *et al* developed a special optical tweezer system called the optical stretcher [6]. The combination of the stretcher with microfluidic networks allowed for the elastic screening of cells. Using the optical stretcher, it was determined that cancer cells are generally softer than normal cells. Recently, the group of Guck applied this method to the diagnosis of oral cancer [7]. The micropipette aspiration technique was used by Ward *et al* to show that cells transformed with Ras-T24 oncogene exhibiting increased tumorigenicity also had increased deformability [8]. Another very promising technique to measure the mechanical properties of cells is particle-tracking microrheology, introduced by the Wirtz group [9] (for an extensive recent review, see [10]). With this method, also called nanorheology, the local viscoelastic properties of a living cell can be probed by the analysis of the movement of sub-micrometer fluorescent beads injected into the cell. This technique allows simultaneous measurement of local mechanical properties with high spatial resolution at different places inside the cell.

Another approach, which allows measurement of local as well as cell-wide mechanical properties, is atomic force microscopy (AFM) [11]. The stiffness of cells can be determined with high lateral resolution by using a sharp AFM tip as a probe. For these experiments, cells are adhered to a surface and a sharp AFM tip is pushed into the cell surface, while the indentation depth and probe deflection are recorded. AFM was used to map the stiffness (Young’s modulus) of a cell during proliferation [12]. This method has also been applied to different cancer cells, and in agreement with the optical stretcher data, cancer cells were found to be a factor 2–10 softer than benign cells [13–15]. For benign (MCF-10A)

and cancerous (MCF-7) breast cell lines, it was reported that the Young’s moduli depend on the loading rate (i.e. the rate at which force is applied) [16]. Alternatively, a micrometer-sized sphere on the AFM cantilever can be used to measure the global mechanical properties of the cell [17, 18]. The Hertz model [19], describing the simple case of the deformation of two perfectly homogeneous smooth bodies touching under load, is most commonly used for the analysis of AFM-based cell mechanical experiments [20]. For thin samples such as areas in the lamellipodia, Mahaffey *et al* used the Chen and Tu extensions of the Hertz model to get the storage and loss moduli of adhered and non-adhered regions, respectively [17].

In this paper, we present findings from our study of the local mechanical properties of the nuclear regions of esophageal cell lines in different phases of premalignancy. We compared cells from a normal squamous cell line (EPC2) [21] and two Barrett’s Esophagus columnar cell lines (CP-A and CP-D) and also studied the influence of organic dyes on their mechanical properties. CP-A was derived from biopsies taken from a region of non-dysplastic metaplasia and CP-D was derived from biopsies taken from regions of high-grade dysplasia [22]. Previous cytogenetic studies have revealed p16 deletion and wild-type p53 in CP-A, and both p16 and p53 deletion in CP-D. The cell lines were shown to be karyotypically similar to *in vivo* counterparts [22, 23]. To the best of the authors’ knowledge, this is the first comparative elasticity study of premalignant cells.

For our experiments, we used a combination of an AFM with a confocal laser scanning microscope (CLSM) capable of measuring the fluorescence lifetimes of the dyes (fluorescence lifetime imaging microscopy, FLIM) (figure 1(a)). The ability to move the sample and objective independently allows for precise alignment of the AFM probe and laser focus with an accuracy down to a few nanometers [24]. This enables

direct correlation of the point of indentation and the sub-cellular structures in the FLIM image. To apply the Hertz model to heterogeneous materials like cells, we developed algorithms for the segmental analysis of force-indentation curves. This enables the quantification of stiffness as it varies with indentation depth (figures 1(b) and (c)).

## 2. Materials and methods

### 2.1. Cell culture

Immortalized Barrett's Esophagus (BE) cells derived from non-dysplastic metaplasia (CP-A cells) and high-grade dysplasia (CP-D cells) [22, 23] and normal esophageal cells (EPC2 cells) were used for the experiments. Cells from all studied cell lines were cultured in Keratinocyte-serum-free medium 1  $\times$  (Invitrogen, Carlsbad, CA). The medium contained L-glutamine and calcium chloride. Additional supplements added to the medium prior to use were bovine pituitary extract (1  $\times$  25 mg, Invitrogen) and epidermal growth factor—human recombinant (1  $\times$  2.5  $\mu$ g, Invitrogen).

### 2.2. Sample preparation

The cultured cells were then seeded at  $\sim$ 30% confluence into 50 mm glass bottom petri dishes (Fluorodish, World Precision Instruments) and incubated with growth medium at 37  $^{\circ}$ C and 5% CO<sub>2</sub> for a period of 72 h. The medium was exchanged with 1 ml imaging assay buffer (Enzo Life Sciences) prior to AFM measurements to provide an optically clear medium optimized for fluorescence imaging. The solution was also buffered for CO<sub>2</sub> and pH 7.5 by adding 25 mM HEPES. For experiments on stained cells, 5  $\mu$ l of 1:5 diluted stock solution of Nuclear ID Red (Enzo Life Sciences) and 5  $\mu$ l of 1:5 diluted stock solution of Nucleolar ID Green (Enzo Life Sciences) were added to the medium 30 min prior to AFM measurements and allowed to diffuse with gentle swirling.

### 2.3. Combined AFM–CLSM setup

The combined AFM–CLSM setup we used consists of a sample scanning AFM (MFP-3D Bio, Asylum Research, CA) and a single molecule sensitive confocal fluorescence microscope (Microtime 200, PicoQuant, Germany), equipped with 470 nm and 640 nm lasers for excitation, a high-end 100  $\times$  1.45 NA oil immersion objective (Olympus, San Diego, CA) and two single-photon counting modules for detection [24]. The mechanical link between the two systems is the AFM sample stage, which is mounted onto an Olympus IX-71 inverted microscope. With this setup, the fluorescence dynamics can be followed on time scales from sub-nanoseconds to seconds. This setup is ideal for FLIM. The underlying technique (time-tagged time-resolved single photon recording) allows us to simultaneously record timing and fluorescence intensity information, both spectrally and spatially resolved, on a single photon basis. While the sample scanning AFM acts as master, the parallel time-correlated single-photon counting (TCSPC) data acquisition serves as a slave: start and stop scan line information from

the AFM are transferred to the TCSPC electronics, enabling us to achieve online synchronized and matched AFM and fluorescence images with direct access to ns time-resolved single-photon data.

### 2.4. AFM nanoindentation

Soft silicon AFM probes with nominal spring constants  $k \approx 10$  pN nm<sup>-1</sup> (MSNL, Veeco Instruments, Santa Barbara, CA) were used for the indentation experiments. The spring constant of each cantilever was determined from the thermal noise spectrum [25, 26]. The AFM tip and the confocal volume were aligned using the pattern of back-scattered light [24]. After the alignment, the AFM tip is fully retracted and the sample stage is moved until a cell of interest is under the tip. A FLIM image of the cell in two frequency bands (green and deep red) is acquired while the tip is still retracted. In the FLIM image, the cell nucleus is identified and precisely located. The nucleus is brought directly under the AFM tip. In a ( $\sim$ 5  $\mu$ m)<sup>2</sup> region, an 8  $\times$  8 grid of indentations is acquired with 2  $\mu$ m s<sup>-1</sup> approach and retract speeds in force volume mode with a trigger force of 1 nN. After indentation, a subsequent FLIM image is taken of the cell with exactly the same settings as the preliminary image. The two images are superposed in software (ImageJ [27]) to determine the extent to which the cell moved during the measurements. If the cell moved more than  $\sim$ 1  $\mu$ m, then the data are discarded and are not further analyzed. The alignment of the tip is then verified as above and another cell can be located and measured. After measurements, the probes were imaged with a scanning electron microscope and the tip radii were determined to be in the range of 50 nm.

### 2.5. Data analysis

Each indentation generates a force-indentation ( $F$ - $\delta$ ) curve to be saved and analyzed with custom written software (Igor Pro, Wavemetrics, Portland, OR). The curves are corrected for cantilever bending. All force data points are incremented by a constant so that they are all positive, subsequently raised to the 2/3 power and then plotted in a  $F^{2/3}$ - $\delta$  curve. According to the Hertz model [19] of a sphere indenting an elastic half-space, the Young's modulus  $E$  is directly proportional to the force  $F$  and inversely proportional to the 3/2 power of the deformation  $\delta$ :

$$F = \frac{4}{3} \frac{E}{(1 - \nu^2)} \sqrt{\delta^3 R},$$

where  $F$  is the load distributed over the contact area,  $R$  is the radius of the sphere,  $\nu$  is the Poisson ratio of the surface,  $\delta$  is the deformation of the sample and  $E$  is the Young's modulus of the sample. Here, the AFM tip is approximated as a sphere of radius  $R$  on a cantilever deflected by a force  $F$ . The cell is approximated as a flat, isotropic material with a Poisson ratio of 0.4 that is elastically deformed by the AFM tip in the limit of small strains [28]. Accordingly, the  $F^{2/3}$ - $\delta$  curve should be linear [29], with a slope directly proportional to  $E^{2/3}$ :

$$\frac{\Delta F^{2/3}}{\Delta \delta} = \left( \frac{4}{3} \frac{E}{(1 - \nu^2)} \sqrt{R} \right)^{2/3}.$$

In practice, however, the  $F^{2/3}$ - $\delta$  curves generated by AFM-based nanoindentation are not simply linear. Rather, linear segments corresponding to layers with different stiffness can be seen at different depths. We therefore invoke a robust piecewise linear fitting algorithm to reconstruct the curves into segments of constant Young's modulus  $E(\delta)$  at different depths. The algorithm works by first fitting a line in a small region of the curve and then iteratively extrapolating it until a parameter-sensitive deviation threshold is exceeded. Then another small line is fitted in the adjacent region and the process repeats until the whole curve is fitted. The algorithm first fits the baseline and determines the contact point in this manner, and then fits the indentation region. It is worth noting that determination of the contact point is critical in AFM force-indentation analyses, but our scheme is less sensitive to errors in contact point determination than those that fit power curves from the contact point through the entire indentation.

To characterize statistical distributions, we used a kernel smoothing density estimate function ('ksdensity.m', Matlab, Mathworks, Natick, MA).

### 3. Results and discussion

#### 3.1. Combined AFM-nanoindentation and CLSM

For the nanoindentation experiments, we used a combined AFM-CLSM setup, which allows the alignment of the AFM tip with the confocal volume, resulting in a precise correlation of the fluorescence images and the point of indentation. AFM tips with tip radii of  $\sim 50$  nm were used in order to get precise alignment and to probe the mechanical responses at the nanoscale. Figure 1(a) shows a schematic of AFM-CLSM cell indentation. The AFM tip is cycled up and down while the force acting on the tip is recorded. Figure 1(b) shows representative force-indentation curves ( $F$ - $\delta$  curves). To fit the Hertz model, data points are plotted in the  $F^{2/3}$ - $\delta$  curves (figure 1(c)), whose slopes are proportional to  $E^{2/3}$ . The curves show different slopes, requiring the calculation of depth-dependent Young's moduli. In figure 1(c), the blue curve from a normal squamous EPC2 cell shows a steep incline after the tip hits the cell surface, representing stiff behavior at this point. In contrast, compliant behavior is exemplified by the orange curve from a dysplastic CP-D cell stained with organic dyes. We also observed curves whose slopes increase non-monotonically (green, CP-A unstained) and saw-tooth patterns (red, CP-D unstained).

In order to precisely localize the cell nuclei and nucleoli, we chose to employ FLIM rather than regular fluorescence because of its higher contrast. The lifetimes of the fluorophores' excited states depend on the decay pathways available, which are sensitive to any number of highly localized environmental conditions that might influence the cell's mechanical properties [30]. Figure 2 shows fluorescence lifetime images of a single CP-D cell stained with nuclear and nucleolar dyes, in its entirety (figure 2(a)) and in a close-up of the nucleus (figure 2(b)). The images integrate data from the emission spectra of both dyes. The intensity of photons in each pixel is represented by the brightness of

**Table 1.** Kernel smoothing density estimates of modal Young's moduli and distribution full widths at half maxima (FWHM) from figure 3.

Cell type	Number of cells	Total number of indentations	Modal Young's modulus (kPa)	FWHM (kPa)
EPC2 unstained	18	1152	4.72	7.17
CP-A unstained	10	640	3.08	5.64
CP-D unstained	19	1216	2.64	5.49
EPC2 stained	5	320	9.89	17.96
CP-A stained	5	320	2.98	7.04
CP-D stained	16	1024	2.12	5.65

the pixel, and the average lifetime of photons detected in each pixel is represented by the color. Different fluorescence lifetimes of the two dyes allow the superposition of the two image channels. In figure 2(a), distinct chromatin fibers in the nucleus are light blue-green in color. Small blue ellipses in the cytoplasm indicate mitochondrial DNA. The shorter lifetime of mtDNA may be due to lower pH in the mitochondrial matrices. In figure 2(b) the nucleoli are yellow-red. A topography map of the same field of view is shown in figure 2(c). The cell is indented 64 times in an  $8 \times 8$  grid. In each indentation, the AFM probe presses into the cell until 1 nN of force is applied, whereupon the tip is retracted. The vertical position of the AFM cantilever at maximum indentation is plotted to visualize a stiffness-dependent measure of its height. The Young's modulus of the final fit line in the  $F^{2/3}$ - $\delta$  curve from each indentation in 2(b) is plotted in figure 2(d). The stiffness of the cell is clearly heterogeneous on length scales of  $\sim 1 \mu\text{m}$ . No obvious correlation can be seen between the fluorescence image and the AFM data, perhaps because the nuclear membrane redistributes the load applied by the tip. The central nuclear region exhibits soft spots, while the nuclear membrane in the bottom corners appear stiffer.

#### 3.2. Mechanical properties for deep indentations

To investigate and compare the elasticities of the nuclei of EPC2, CP-A and CP-D cells, nuclei from several cells were indented 64 times each in  $8 \times 8$  grids in  $(\sim 5 \mu\text{m})^2$  areas. The Young's moduli of the final fit lines were calculated. The six distributions of moduli from the three different cell lines, both unstained (figure 3(a)) and stained (figure 3(b)), were assessed with a kernel smoothing density (KSD) algorithm. Supplementary figure 1 available from [stacks.iop.org/PhysBio/8/015007/mmedia](http://stacks.iop.org/PhysBio/8/015007/mmedia) demonstrates that the KSD characterizes the distributions very well. Because there is yet no specific model for the distribution of Young's moduli at the spatial resolution of AFM-based nanoindentation, we use the KSD as a model-independent statistical estimate of the modal Young's modulus and

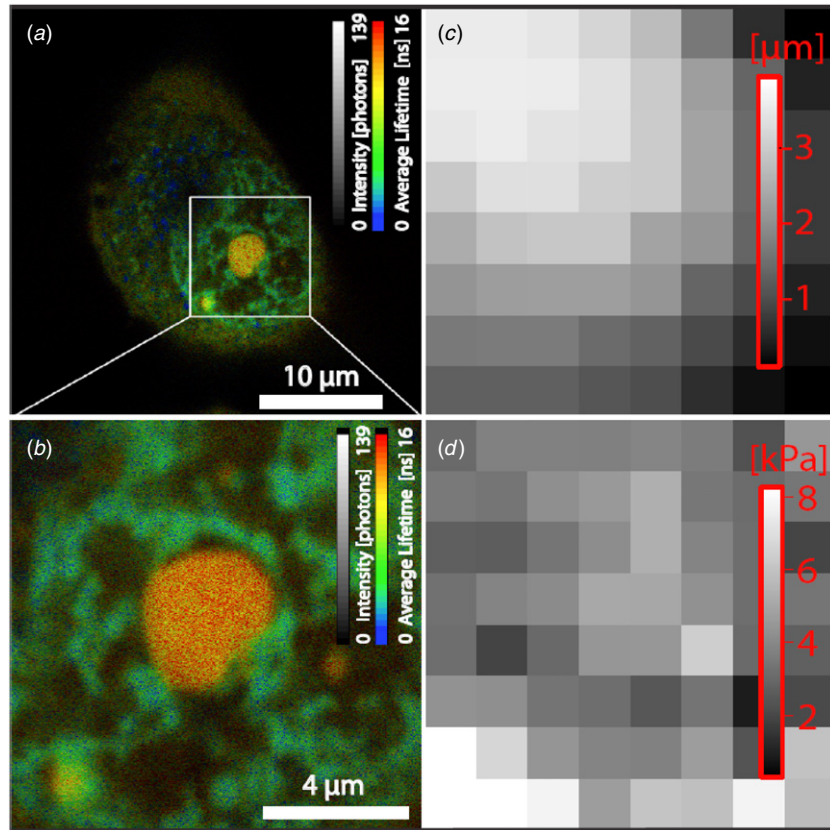


**Figure 2.** Adherent dysplastic CP-D esophageal cell analyzed with combined fluorescence lifetime imaging and AFM-based nanoindentation. Confocal fluorescence lifetime images of the cell labeled with nuclear dye emitting in red and nucleolar dye emitting in green (a) in its entirety and (b) in a close-up of the nucleus. Pixels are color mapped to average fluorescence lifetime and intensity mapped to photon count. The AFM tip is aligned with the confocal volume before scanning. Topography (c) and elasticity (d) from  $8 \times 8$  AFM force map of the same area as (b) with a trigger force of 1 nN. Height is calculated from the AFM cantilever's vertical position at maximal indentation. Young's moduli are calculated with the Hertz model from the final region of each force-indentation curve.

distribution width (see table 1). The modal Young's modulus of unstained EPC2 was 4.7 kPa, and those of unstained CP-A and CP-D were 3.1 kPa and 2.6 kPa, respectively. The non-dysplastic CP-A cells in this study are thus softer than the normal EPC2 cells by a factor of  $\sim 1.5$ , while the dysplastic CP-D cells are softer by a factor of  $\sim 1.8$ . These noteworthy premalignant variations in stiffness suggest that mechanical compliance increases gradually along with the morphological changes marking the progression from metaplasia to neoplasia. The changes in compliance we found complement previous reports that malignant cells are softer than their normal counterparts by factors ranging from 2 to 4 [13, 14, 16].

We also tested the influence of nuclear and nucleolar dyes on the mechanical properties of the cells (figure 3(b)). For EPC2 cells stained with Nuclear ID Red and Nucleolar ID Green, significant stiffening was found (9.9 kPa). This is in accordance with single cell compression experiments on cells stained with various cell tracing dyes [31]. In contrast, the stained CP-A showed no clear trend (2.9 kPa) and a slight softening was observed (2.1 kPa) in the case of stained CP-D. We speculate that this surprising effect reflects systemic differences in the metabolic and regulatory processes that govern cytoskeletal stability in the abnormal cell lines.

### 3.3. Segmental analysis of force-indentation curves

To better understand the nature of the mechanical differences between these cells, we analyzed the force-indentation curves to get the Young's modulus as a function of the indentation depth. In contrast to curve fitting approaches [32, 33], our algorithm detects Hertzian-like segments and analyzes the Young's modulus, depth and length of these segments. Figures 4(a) and (b) depict 3D elasticity maps of CP-A and CP-D cells, respectively. The surface heights and Young's moduli are calculated from force maps as in figure 2. The surface is color mapped to the Young's modulus. Additionally, three horizontal black lines are projected on the surface of each cell. These lines correspond spatially to the elasticity tomograms in figures 4(c) and (d). Each tomogram consists of 32 vertical stacks. Each stack contains information about a single indentation. The top of each stack corresponds to the height at which the AFM tip first contacts the cell, as estimated by the linear piecewise fitting algorithm. Each colored band corresponds to the Young's modulus from a single linear segment fitting a region of the  $F^{2/3}-\delta$  curve. The bottom of the stack corresponds to the depth at which the trigger force is reached, and is therefore the same color as the corresponding position of the surface in figures 4(a) or (b). The greater

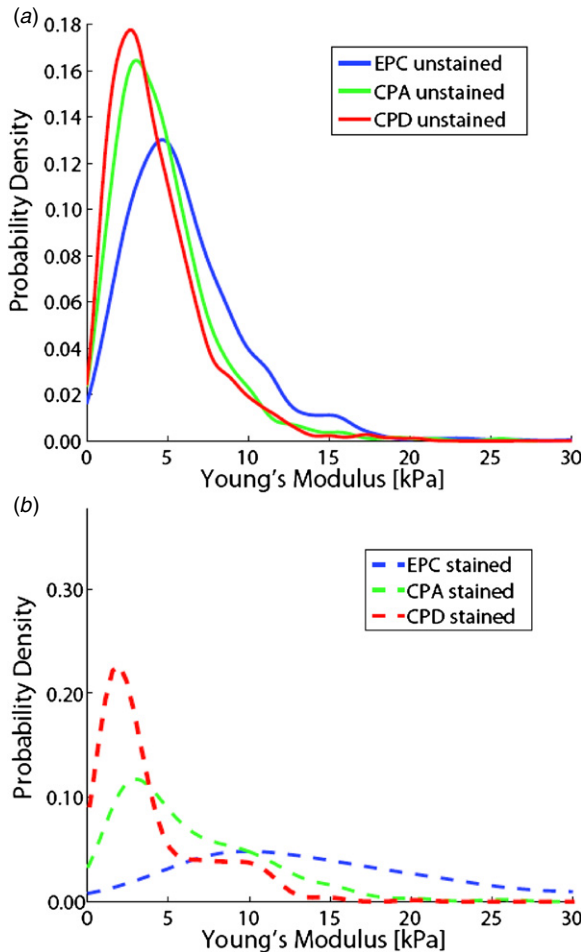


**Figure 3.** Distributions of Young's moduli of EPC2, CP-A and CP-D esophageal cell nuclei. Kernel smoothing density estimates of Young's moduli calculated from the final region of each (of  $n$ ) force-indentation curves collected from  $8 \times 8$  force maps of cell nuclei. FLIM images are taken (before) to identify nuclei and determine scanning region ( $\sim 5 \mu\text{m}^2$ ) of the force maps and (after) to verify that cell has not moved appreciably ( $\leq 1 \mu\text{m}$ ) during measurement. Data from (a) unstained EPC2 ( $n = 1152$ ), CP-A ( $n = 640$ ) and CP-D ( $n = 1216$ ) cell nucleus indentations. The modal Young's modulus is highest for EPC2, intermediate for CP-A and lowest for CP-D (see table 1). Data from (b) EPC2 ( $n = 320$ ), CP-A ( $n = 320$ ) and CP-D ( $n = 1024$ ) cells labeled with both nuclear and nucleolar dyes indicate that with these dyes, the modal Young's modulus of EPC2 increases by a factor of 2, that of CP-A is unchanged and that of CP-D decreases slightly (see table 1).

heights of the CP-D vertical stacks indicate that the CP-D cell is more deformable than the CP-A cell. The CP-D cell appears to be more laterally mechanically homogeneous than the CP-A cell, as indicated by the nearly uniform distribution of yellow bands beginning at about 80% of the total indentation depth. Neither cell is mechanically homogeneous radially, especially as evidenced by the multitude of extremely narrow white bands, representing negative slopes on the  $F^{2/3}-\delta$  curve (breakthrough events, see below).

Because the  $F^{2/3}-\delta$  curves of living cells are so frequently not simply linear, but rather piecewise linear, a single cited value for the Young's modulus of a cell cannot accurately express the cell's elasticity. We therefore plot Young's moduli

as a function of indentation depth in the form of 2D histograms in figure 5. These histograms quantify the depth dependence of cell stiffness and illustrate important differences between these cell lines that cannot be distinguished by nominal depth-independent values of Young's moduli. The starting depth, stopping depth and slope of each linear segment from each  $F^{2/3}-\delta$  curve are used to bin the segments horizontally by indentation depth into 25 nm bins and vertically by the Young's modulus calculated from their slopes into 50 bins spaced logarithmically over five decades, up to 100 kPa. Each segment exceeding 25 nm indentation spans multiple bins. The histograms are color mapped by counts per bin. Segments with negative slopes are excluded.

On each histogram, we have superposed a black curve plotting the  $(E, \delta)$  coordinate solutions of the Hertz equation for  $F = 1$  nN. Because our measurements are performed with a fixed trigger force, an ideal Hertzian cell with constant Young's modulus (as in figure 1(c), blue  $F^{2/3}-\delta$  curve) would occupy a horizontal band of bins spanning from the vertical axis to the Hertz curve. A cell of lower (higher) Young's modulus will be indented more (less). The curve thus provides a point of comparison for the way each cell line differs from an ideal Hertzian cell. A stress hardening cell with monotonically increasing Young's modulus (as in figure 1(c), orange  $F^{2/3}-\delta$  curve) should occupy bins forming a convex curve on the histogram, contributing to the portion of the distribution near the origin. A cell with non-monotonic changes in Young's moduli (as in figure 1(c), green and red  $F^{2/3}-\delta$  curves) occupies bins in a more complicated pattern, contributing to the portion of the distribution to the right of the Hertz curve.

The degree to which the Young's modulus varies with indentation depth differs significantly among the cell lines and with the addition of fluorescent dyes. Data from ( $n$ ) indentations on ( $m$ ) cells are shown: unstained (a) EPC2 ( $n = 1152$ ,  $m = 18$ ), (b) CP-A ( $n = 640$ ,  $m = 10$ ), (c) CP-D ( $n = 1216$ ,  $m = 19$ ); and stained (d) EPC2 ( $n = 320$ ,  $m = 5$ ), (e) CP-A ( $n = 320$ ,  $m = 5$ ) and (f) CP-D ( $n = 1024$ ,  $m = 16$ ). In the case of (a) unstained EPC2, the red horizontal band of peaks at  $\sim 5$  kPa is somewhat Hertzian. However, many EPC2  $F^{2/3}-\delta$  curves show hardening with depth. Unstained CP-D (c) exhibits an isolated cluster (in contrast to a horizontal band) of peaks from  $\sim 1$  to 2 kPa. The characteristic total indentation depths can be estimated by looking at how far to the right each distribution spreads. The bright blue region of the CP-D distribution is very broad and extends considerably past the Hertz curve to  $\sim 1500$  nm. The bright blue region of the EPC2 distribution extends only to  $\sim 800$  nm. The CP-D cells are evidently much more deformable than the EPC2 cells, irrespective of the calculated Young's moduli. Typical cell heights ranged from 7 to  $13 \mu\text{m}$ , depending on size and shape, corresponding to strains  $\sim 10\%$ . Interestingly, the dyes had adverse effects on the different cell lines. The dye apparently caused a decrease in deformability and increase in stiffness of EPC2, opposite effects on CP-D, and an increase in deformability but no change in stiffness in the case of CP-A.

The strain borne by a cell during indentation is clearly not a simply linear function of the stress. Moreover,

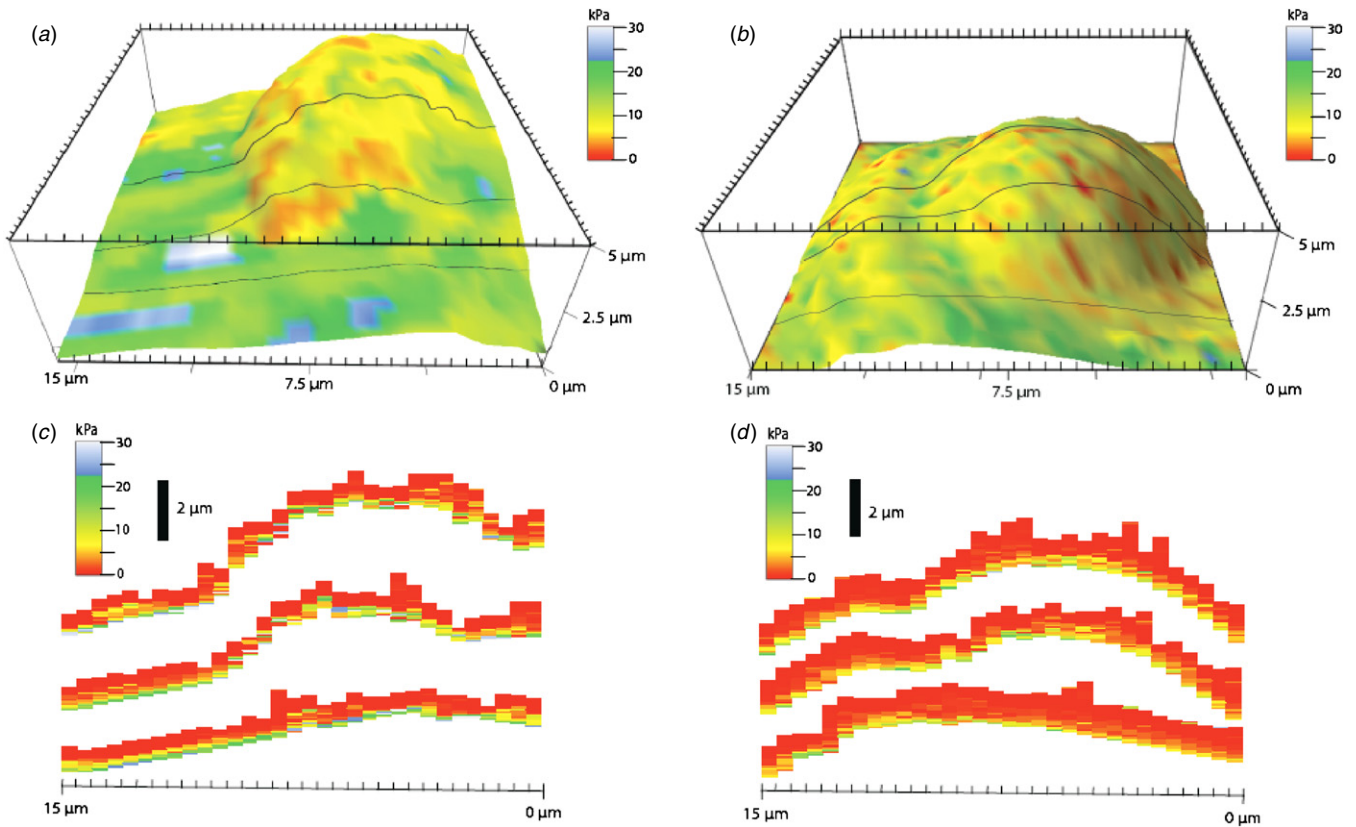


**Figure 4.** 3D elasticity maps and corresponding elastic tomograms of CP-A and CP-D cells. 3D elasticity maps of typical (a) CP-A and (b) CP-D cells. Height and Young's moduli are calculated as in figure 2. The black lines on surfaces correspond to the elasticity tomograms shown in (c) and (d). Surfaces and tomograms are color mapped to Young's modulus. In a tomogram, each vertical rectangular stack depicts a single indentation. The AFM tip contacts the cell at the top and retracts at the bottom of each stack. Tall (short) stacks occur at points where the cell is more (less) deformable. The white bands in the stack indicate breakthrough events (see figure 6). The CP-D cell not only has a lower Young's modulus toward the end of the indentation, but it is also more homogeneous and more deformable than the CP-A cell.

the distributions exhibit neither simple strain hardening nor softening, but rather a mixture of the two. These changes in stiffness could possibly reflect either active rearrangement in which stretch-induced membrane stress activates Rho signalling [34], or passive rearrangement in which the applied load causes geometrical changes such as buckling [31]. The nanoscale details of the cytoskeleton's response to nanoindentation remain unknown, but further development of combined fluorescence techniques may shed light on the processes involved.

### 3.4. Discontinuities in the force-indentation curves

In order to further investigate this nonlinearity we focused on segments of the  $F^{2/3}-\delta$  curves that exhibit negative slopes. Linear segments of  $F^{2/3}-\delta$  curves with negative slope occur when the resistance levied by the cell against the AFM tip is suddenly relieved, allowing it to descend further into the cell with less applied force. An example of this is shown in figure 6(a). In most cases, the segments of negative slope reflect large changes in applied force over very small distances. We propose that these changes correspond to events in which stresses induced by the AFM tip on cortical structures are transferred by intermediate

filaments to stress fibers deeper in the cytoskeleton that break, ultimately allowing superficial material to displace or slip past the disrupted filamentous matrix. We therefore denote such occurrences 'breakthrough events'. The number of breakthrough events can thus be seen as a measure of structural integrity. We expect that breakthrough events should be most frequent in cells with cytoskeletons weakened, for example, by underexpression of actin-binding proteins (ABPs) such as filamin A, downregulation of which is known to occur following the differentiation of neuronal cells [35], and may likewise occur following metaplastic transformation. Apart from its structural role as an actin crosslinker, filamin has been shown to modulate epidermal growth factor receptors (EGFR) [36], which are known to be deregulated in squamous malignancies [21]. We found that the frequency of incidence of breakthrough events differs significantly between the normal EPC2, metaplastic CP-A and dysplastic CP-D cells. Figure 6(b) shows the percentages of total indentations exhibiting 1, 2, 3 and 4 or more breakthroughs for stained and unstained cells of each cell type. The probability of observing breakthrough events increases considerably from EPC2 to CP-A to CP-D. The probability of multiple breakthroughs follows the same pattern of increase. This observation

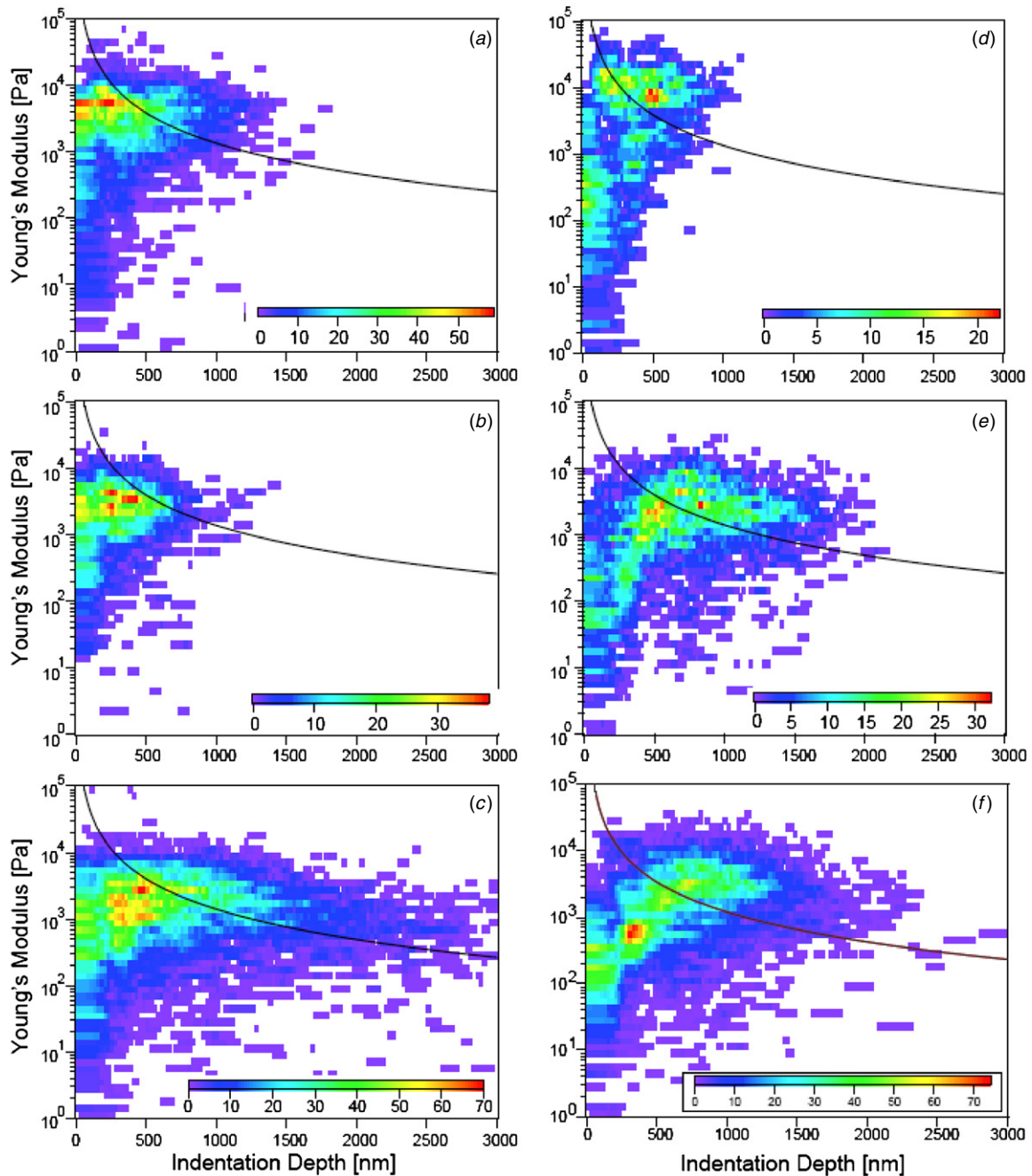


**Figure 5.** 2D elasticity histograms of Young's modulus versus indentation depth. The  $F^{2/3}-\delta$  curves are reconstructed piecewise with linear segments. The starting depth, stopping depth and slope of the linear segments are then used to construct a 2D histogram of Young's modulus versus indentation depth. Each segment is binned horizontally by indentation depth into 25 nm bins and vertically by the Young's modulus calculated from its slope into 50 bins spaced logarithmically over five decades, up to 100 kPa. The histograms are color mapped by counts per bin. Unstained (a) EPC2 ( $n = 1152$ ), (b) CP-A ( $n = 640$ ), (c) CP-D ( $n = 1216$ ) cells and stained (d) EPC2 ( $n = 320$ ), (e) CP-A ( $n = 320$ ) and (f) CP-D ( $n = 1024$ ) cells are shown. The black curve plotting the  $(E, \delta)$  coordinate solutions of the Hertz equation for  $F = 1$  nN applied force. Hertzian behavior (i.e. depth-independent moduli) is characterized by horizontal bands of uniformly occupied bins, such as the red peak in (a) at 5 kPa from 0 to 400 nm. The degree to which the Young's modulus varies with indentation depth differs significantly among the cell lines and with the addition of fluorescent dyes.

suggests that the microscopic explanation for the increased compliance of cancerous and pre-cancerous cells may lie in their susceptibility to 'crumble and yield' rather than their ability to 'bend and flex'.

We also expected that cells with greater structural integrity should require a greater applied force in order for the AFM

tip to elicit a breakthrough. When we summed the changes in force  $\Delta F$  from each breakthrough to get the total breakthrough force from a single indentation, and compared  $\sum \Delta F$  of those curves exhibiting at least one breakthrough, we found no clear difference between the cell lines (supplementary figure 2 available from [stacks.iop.org/PhysBio/8/015007/mmedia](http://stacks.iop.org/PhysBio/8/015007/mmedia)).

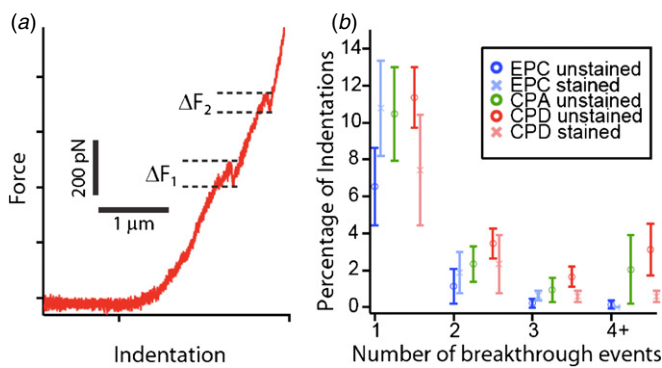


**Figure 6.** Nanoscale cytoskeletal instability quantified by the frequency of incidence of breakthrough events. Linear segments of  $F^{2/3}-\delta$  curves with negative slope occur when the resistance levied by the cell against the AFM tip is suddenly relieved, allowing it to descend further into the cell with less applied force. We propose that these ‘breakthrough events’ correspond to disruptions of pre-stressed tensile structures in the cytoskeletal mesh due to transverse compression by the AFM tip. The percentages of indentations with (exactly) 1, 2, 3 and 4 or more breakthrough events are plotted. Breakthrough events are most frequent in the CP-D cells, as corroborated by the multitude of narrow white bands in the elasticity tomograms in figure 4(d). Interestingly, CP-D exhibited more and EPC2 exhibited less breakthroughs with the use of the nuclear and nucleolar dyes.

Since only a modest percentage of the measured curves exhibited breakthroughs, larger sample sizes may be necessary to see a trend in these data.

#### 4. Conclusion and outlook

Metaplastic CP-A and dysplastic CP-D precancerous esophageal cells were found to be significantly softer than normal EPC2 cells. Additionally, staining the nuclei and the nucleoli with organic dyes was found to produce adverse effects on the mechanical properties of the different cell lines: EPC2 showed significant stiffening, while CP-A showed greater deformability and CP-D showed softening. Correlations between stiffness and the spatial arrangement of chromatin fibers or nucleoli in the nucleus were not evident; however, labeling other subcellular structures might reveal correlations in future work.

We also developed a robust piecewise linear fitting algorithm to determine indentation depth-dependent Young’s moduli. Our segmental analysis of force-indentation curves was used to clarify distinctions between stiffness and deformability in cells with nonlinear strain-hardening. In stiffness tomograms and 2D histograms, we identified subtle differences in the distributions of the mechanical properties of the cell lines. Divergence from Hertzian behavior was assessed in terms of  $F^{2/3}-\delta$  curves whose slopes increase non-monotonically. The frequency of segments with negative slope (‘breakthroughs’) in AFM force-indentation curves may also prove to be a useful parameter in the characterization of cytoskeletal stability.

Even in the earliest stages of cancer development, the mechanical properties of the cell are altered. This study,

conducted on a cell line model of pre-neoplastic progression in the human esophagus, suggests that the correlation between increased elasticity and malignancy holds even in the early stages of metaplastic transformation. While measurements on explanted cells would strengthen the case, our results are consistent with the growing body of evidence from a variety of different experimental techniques and cell types that cells in later stages of many cancers are abnormally soft.

To gain deeper cytomechanical insight, more sophisticated models must face the structural and morphological heterogeneity of the cell head on. Possible approaches are finite element methods [37, 38] or subcellular element models [39]. With the development of appropriate analytical techniques, the AFM shows promise in its ability to probe the elasticity of cells even deep within the cytoskeleton. Future developments of quantitative mechanical nanotomography methods will not only facilitate better understanding of mechanical properties deep within the cell, it will also illuminate the authentic mechanics of cells in more physiological conditions by rendering possible the elastic analysis of cells embedded in ECM-like matrices.

#### Acknowledgments

The authors acknowledge support from NIH (U54 CA143682) and Arizona State University. JRS was supported by GAANN (P200A090123). The esophageal epithelial cell lines were kindly provided by Dr Carlo Maley. We thank Patti Senechal-Willis and Courtney Hemphill for their assistance with cell culture and sample preparation. We gratefully acknowledge the use of the SEM facilities within the Center for Solid State Science at Arizona State University. We thank Olaf Schulz for help with the combined AFM/CLSM setup and determination of the AFM tip radii with SEM. The help of Dr Felix Koberling, Dr Marcelle Koenig, (PicoQuant GmbH) and Dr Deron Walters, Jacob Viani (Asylum Research) in the synchronization of the AFM with the FLIM setup is gratefully acknowledged.

#### References

- [1] Paszek M J *et al* 2005 Tensional homeostasis and the malignant phenotype *Cancer Cell* **8** 241–54
- [2] Fraley S I, Feng Y F, Krishnamurthy R, Kim D H, Celdon A, Longmore G D and Wirtz D 2010 A distinctive role for focal adhesion proteins in three-dimensional cell motility *Nat. Cell Biol.* **12** 598–U169
- [3] Kasas S *et al* 2005 Superficial and deep changes of cellular mechanical properties following cytoskeleton disassembly *Cell Motil. Cytoskeleton* **62** 124–32
- [4] Huang S and Ingber D E 2005 Cell tension, matrix mechanics, and cancer development *Cancer Cell* **8** 175–6
- [5] Suresh S 2007 Biomechanics and biophysics of cancer cells *Acta Biomaterialia* **3** 413–38
- [6] Guck J *et al* 2005 Optical deformability as an inherent cell marker for testing malignant transformation and metastatic competence *Biophys. J.* **88** 3689–98
- [7] Remmerbach T W, Wottawah F, Dietrich J, Lincoln B, Wittekind C and Guck J 2009 Oral cancer diagnosis by mechanical phenotyping *Cancer Res.* **69** 1728–32

- [8] Ward K A, Li W I, Zimmer S and Davis T 1991 Viscoelastic properties of transformed-cells—role in tumor-cell progression and metastasis formation *Biorheology* **28** 301–13
- [9] Tseng Y, Kole T P and Wirtz D 2002 Micromechanical mapping of live cells by multiple-particle-tracking microrheology *Biophys. J.* **83** 162–76
- [10] Wirtz D 2009 Particle-tracking microrheology of living cells: principles and applications *Annu. Rev. Biophys.* **38** 301–26
- [11] Radmacher M 1997 Measuring the elastic properties of biological samples with the AFM *IEEE Eng. Med. Biol. Mag.* **16** 47–57
- [12] Matzke R, Jacobson K and Radmacher M 2001 Direct, high-resolution measurement of furrow stiffening during division of adherent cells *Nat. Cell Biol.* **3** 607–10
- [13] Cross S E, Jin Y S, Rao J and Gimzewski J K 2007 Nanomechanical analysis of cells from cancer patients *Nature Nanotechnol.* **2** 780–3
- [14] Cross S E, Jin Y S, Tondre J, Wong R, Rao J and Gimzewski J K 2008 AFM-based analysis of human metastatic cancer cells *Nanotechnology* **19** 384003
- [15] Lekka M, Laidler P, Gil D, Lekki J, Stachura Z and Hrynkiwicz A Z 1999 Elasticity of normal and cancerous human bladder cells studied by scanning force microscopy *Eur. Biophys. J. Biophys. Lett.* **28** 312–6
- [16] Li Q S, Lee G Y H, Ong C N and Lim C T 2008 AFM indentation study of breast cancer cells *Biochem. Biophys. Res. Commun.* **374** 609–13
- [17] Mahaffy R E, Park S, Gerde E, Kas J and Shih C K 2004 Quantitative analysis of the viscoelastic properties of thin regions of fibroblasts using atomic force microscopy *Biophys. J.* **86** 1777–93
- [18] Lulevich V, Zink T, Chen H Y, Liu F T and Liu G Y 2006 Cell mechanics using atomic force microscopy-based single-cell compression *Langmuir* **22** 8151–5
- [19] Hertz H 1882 Über den Kontakt elastischer Körper *J. fuer die Reine Angew. Math.* **92** 156–71
- [20] Kuznetsova T G, Starodubtseva M N, Yegorenkov N I, Chizhik S A and Zhdanov R I 2007 Atomic force microscopy probing of cell elasticity *Micron* **38** 824–33
- [21] Andl C D, Mizushima T, Nakagawa H, Oyama K, Harada H, Chruma K, Herlyn M and Rustgi A K 2003 Epidermal growth factor receptor mediates increased cell proliferation, migration, and aggregation in esophageal Keratinocytes *in vitro* and *in vivo* *J. Biol. Chem.* **278** 1824–30
- [22] Palanca-Wessels M C, Barrett M T, Galipeau P C, Rohrer K L, Reid B J and Rabinovitch P S 1998 Genetic analysis of long-term Barrett's esophagus epithelial cultures exhibiting cytogenetic and ploidy abnormalities *Gastroenterology* **114** 295–304
- [23] Palanca-Wessels M C A, Klingelutz A, Reid B J, Norwood T H, Opheim K E, Paulson T G, Feng Z D and Rabinovitch P S 2003 Extended lifespan of Barrett's esophagus epithelium transduced with the human telomerase catalytic subunit: a useful *in vitro* model *Carcinogenesis* **24** 1183–90
- [24] Schulz O, Koberling F, Walters D, Koenig M, Viani J and Ros R 2010 Simultaneous single molecule atomic force and fluorescence lifetime imaging *Proc. SPIE* **7571** 757109
- [25] Hutter J L and Bechhoefer J 1993 Calibration of atomic-force microscope tips *Rev. Sci. Instrum.* **7** 1868–73
- [26] Butt H J and Jaschke M 1995 Calculation of thermal noise in atomic force microscopy *Nanotechnology* **6** 1–7
- [27] Rasband W S 1997–2009 *ImageJ* (Bethesda: U.S. National Institutes of Health) <http://rsb.info.nih.gov/ij/>
- [28] Trickey W R, Baaijens F P T, Laursen T A, Alexopoulos L G and Guilak F 2006 Determination of the Poisson's ratio of the cell: recovery properties of chondrocytes after release from complete micropipette aspiration *J. Biomech.* **39** 78–87
- [29] Guo S L and Akhremitchev B B 2006 Packing density and structural heterogeneity of insulin amyloid fibrils measured by AFM nanoindentation *Biomacromolecules* **7** 1630–6
- [30] Wessels J T, Yamauchi K, Hoffman R M and Wouters F S 2010 Advances in cellular, subcellular, and nanoscale imaging *in vitro* and *in vivo* *Cytometry* **77A** 667–76
- [31] Lulevich V, Shih Y P, Lo S H and Liu G Y 2009 Cell tracing dyes significantly change single cell mechanics *J. Phys. Chem. B* **113** 6511–9
- [32] Roduit C, Van Der Goot F G, Los Rios P, Yersin A, Steiner P, Dietler G, Catsicas S, Lafont F and Kasas S 2008 Elastic membrane heterogeneity of living cells revealed by stiff nanoscale membrane domains *Biophys. J.* **94** 1521–32
- [33] Costa K D, Sim A J and Yin F C P 2006 Non-Hertzian approach to analyzing mechanical properties of endothelial cells probed by atomic force microscopy *Trans. ASME J. Biomech. Eng.* **128** 176–84
- [34] Smith P G, Roy C, Zhang Y N and Chaudhuri S 2003 Mechanical stress increases RhoA activation in airway smooth muscle cells *Am. J. Respir. Cell Mol. Biol.* **28** 436–42
- [35] Sheen V L, Feng Y Y, Graham D, Takafuta T, Shapiro S S and Walsh C A 2002 Filamin A and Filamin B are co-expressed within neurons during periods of neuronal migration and can physically interact *Hum. Mol. Genet.* **11** 2845–54
- [36] Fiori J L *et al* 2009 Filamin A modulates kinase activation and intracellular trafficking of epidermal growth factor receptors in human melanoma cells *Endocrinology* **150** 2551–60
- [37] Kasas S and Dietler G 2008 Probing nanomechanical properties from biomolecules to living cells *Pflugers Arch. Eur. J. Physiol.* **456** 13–27
- [38] Ohashi T, Ishii Y, Ishikawa Y, Matsumoto T and Sato M 2002 Experimental and numerical analyses of local mechanical properties measured by atomic force microscopy for sheared endothelial cells *Biomed. Mater. Eng.* **12** 319–27
- [39] Sandersius S A and Newman T J 2008 Modeling cell rheology with the subcellular element model *Phys. Biol.* **5** 015002